Science Advances
AAAS

Manuscript Template

FRONT MATTER

Title

- Quantifying methane emissions from the largest oil producing basin in the U.S. from space
- Methane Emissions from the Permian Basin

Authors

Yuzhong Zhang[1,2,3,4], Ritesh Gautam[2], Sudhanshu Pandey[5], Mark Omara[2], Joannes D. Maasakkers[5], Pankaj Sadavarte[5,6], David Lyon[2], Hannah Nesser[1], Melissa P. Sulprizio[1], Daniel J. Varon[1], Ruixiong Zhang[7], Sander Houweling[5,8], Daniel Zavala-Araiza[2,9], Ramon A. Alvarez[2], Alba Lorente[5], Steven P. Hamburg[2], Ilse Aben[5], Daniel J. Jacob[1]

Affiliations

[1]School of Engineering and Applied Sciences, Harvard University, Cambridge, Massachusetts, USA.

[2]Environmental Defense Fund, Washington, District of Columbia, USA.

[3]School of Engineering, Westlake University, Hangzhou, Zhejiang Province, China.

[4]Institute of Advanced Technology, Westlake Institute for Advanced Study, Hangzhou, Zhejiang Province, China.

[5]SRON Netherlands Institute for Space Research, Utrecht, the Netherlands.

[6]TNO, Department of Climate, Air and Sustainability, Utrecht, the Netherlands.

[7]School of Earth and Atmospheric Sciences, Georgia Institute of Technology, Atlanta, Georgia, USA.

[8]Department of Earth Sciences, Vrije Universiteit Amsterdam, Amsterdam, the Netherlands.

[9]Institute for Marine and Atmospheric research Utrecht (IMAU), Utrecht University, Utrecht, The Netherlands

Correspondence to-
Yuzhong Zhang (zhangyuzhong@westlake.edu.cn)
Ritesh Gautam (rgautam@edf.org)

Abstract

Using new satellite observations and atmospheric inverse modeling, we report methane emissions from the Permian Basin, which is among the world's most prolific oil-producing regions, and accounts for >30% of total U.S. oil production. Based on satellite measurements from May 2018 to March 2019, Permian methane emissions from oil and natural gas production are estimated to be 2.7±0.5 Tg a^{-1}, representing the largest methane flux ever reported from a U.S. oil/gas producing

region and are >2 times higher than bottom-up inventory-based estimates. This magnitude of emissions is 3.7% of the gross gas extracted in the Permian, i.e. ~60% higher than the national average leakage rate. The high methane leakage rate is likely contributed by extensive venting and flaring resulting from insufficient infrastructure to process and transport natural gas. This work demonstrates a high-resolution satellite data-based atmospheric inversion framework, providing a robust top-down analytical tool for quantifying and evaluating sub-regional methane emissions.

MAIN TEXT

Introduction

Methane is a potent greenhouse gas with a relatively short average atmospheric residence time of about a decade, and is also a precursor of tropospheric ozone (*1*). The emission-based radiative forcing for methane (including effects on tropospheric ozone and stratospheric water vapor) is 0.97 W m^{-2} since preindustrial times, which is about 60% of that for CO_2 (*2*). Roughly a third of the contemporary anthropogenic methane emissions come from the fossil fuel energy sector worldwide (oil, natural gas, and coal) (~ 100–180 Tg a^{-1}) (*3,4,5*). Curbing anthropogenic methane emissions, including those from the oil/gas sector, is considered an effective strategy to slow the rate of near-term climate warming (*1*). However, the rapid increase in oil and natural gas (O/G) production in the U.S. since around 2005, driven primarily by hydraulic fracturing and horizontal drilling, has led to major concerns about increasing methane emissions and adverse climate impacts (*6*). By upscaling data collected from field measurements in some of the largest O/G production basins in the U.S., Alvarez et al. (*7*) estimated 13 Tg annual methane emissions from the national O/G supply chain for 2015, which is 60% higher than the official estimates by the U.S. Environmental Protection Agency (EPA) (*8*). The largest discrepancy was found in the O/G production segment where the estimate by Alvarez et al. (*7*) (7.6 Tg a^{-1}) was more than two times that by EPA which relies on inventory-based estimates (*8*) (3.5 Tg a^{-1}).

While field measurements provide in-depth information about a particular site or area, it is often challenging to expand the measurement capacity to observe a diverse set of targets distributed globally over longer periods of time. Additional challenges exist for areas that are difficult to access for technical or proprietary reasons. On the other hand, global satellite observations of column atmospheric methane offer a unique vantage point to identify emission hotspots and quantify regional emissions (*9*). Using data from SCanning Imaging Absorption spectroMeter for Atmospheric CHartographY (SCIAMACHY) satellite observations averaged between 2003-2009, Kort et al. (*10*) found large anomalous methane levels from the Four Corners region in the U.S., with total methane emissions associated with natural gas, coal and coalbed sources estimated as 0.59±0.08 Tg a^{-1}. While the SCIAMACHY data were fairly limited in spatial resolution (30 km × 60 km) and measurement precision (30 parts per billion in volume or ppbv) (*9*), it was the first time satellite observations were used to quantify a dense O/G related methane emission hotspot. This finding also led to several dedicated airborne studies to better understand methane sources in the region (*11, 12*), which reported methane fluxes comparable to the satellite-based estimate (*10*).

Here, we demonstrate and exploit the capability of a recent space-borne sensor, the Tropospheric Monitoring Instrument (TROPOMI), to map atmospheric methane enhancements in the U.S. and quantify emissions from the Permian Basin (Figure 1), which has become the world's most prolific oil producing regions in recent years due to advances in drilling technologies. Located in New Mexico and Texas in a region of ~400 km × 400 km, Permian is currently the largest oil producing basin in the U.S. In 2018, the Permian Basin produced 5.5×10^5 m^3 (or 3.5 million barrels) of crude oil and 3.2×10^8 m^3 (or 11 billion cubic feet) of natural gas every day (~ 30% and ~10% of the U.S. national totals, respectively), which was 4 and 2.5 times their corresponding levels in 2007 (around the time of SCIAMACHY observations) (Figure 2) (*13*). While the surging production in the Permian Basin and its significance in the U.S. oil boom during the last decade have been widely covered in mass media (*14*), the scale of associated methane emissions from this critical O/G basin are unknown, despite reports of increased flaring and venting activity (*15*).

Using 11 months of recent data acquired by TROPOMI during 2018–2019, we focus on the distinct methane concentration anomaly over the Permian Basin, and quantify the associated methane emissions with a state-of-the-art atmospheric inverse modeling framework. TROPOMI was launched in October 2017 onboard the European Space Agency's Sentinel-5P satellite, and provides column atmospheric methane measurements with higher spatial resolution (7 km × 7 km at nadir) and precision (0.6%) than was previously available (*16*), providing near daily global coverage with its large 2,600 km wide swath (*17*). Our integrated satellite-based approach provides new insights into the dynamic landscape of O/G-related methane emissions in the U.S., and should pave the way forward towards routine quantification, monitoring, and evaluation of methane emissions from source regions distributed globally.

Results

Satellite observations of the Permian Methane Anomaly

Figure 1A shows a map of column-averaged dry-air methane mixing ratio over the conterminous U.S., retrieved from TROPOMI measurements, with correction for the topography effect (denoted as XCH_4^t; see *Methods*). The data are averaged from May 2018 to March 2019. Significant enhancements of XCH_4^t relative to the surrounding background, up to ~ 30 ppbv, are found over the Permian Basin, indicating strong methane emissions. Other notable enhancements are observed in California's central valley, coastal Southeast, and the Mississippi River Valley, likely associated with anthropogenic (agriculture, dairy) and natural (wetland) sources. The elevated methane levels in central California were also seen earlier in the SCIAMACHY analysis (*10*).

The methane enhancements over the Permian Basin show a characteristic two-branch pattern, which aligns with the two major O/G production sub-basins, the Delaware basin to the west and the Midland basin to the east (Figure 1B). The enhancement over the Delaware basin, where extensive new exploitation has taken place during the last five years (*18*) (fig. S1), is larger than that over the Midland basin (Figure 1B). Intensive O/G production activity in these two sub-basins is also captured by satellite observations of radiant heat from gas flaring (Figure 3A; nighttime observations by

VIIRS) and NO_2 tropospheric column densities (Figure 3B; daytime observations by TROPOMI). Flaring is a common practice in O/G operations to burn off unwanted or excess gas, and NO_2 is a gaseous pollutant released during gas flaring and other combustion activities in O/G fields (*19, 20*). Based on measurements by the VIIRS instrument onboard the Suomi National Polar-orbiting Partnership satellite, we estimate an average flaring rate of 5.9±1.2 billion $m^3 a^{-1}$ during the period of this study, about 4.6% of the gross gas production (see text S1). A fourfold increase in flaring intensity since 2012, observed by the VIIRS instrument, is indicative of the rapid growth in O/G production across the Permian Basin (fig. S1).

Methane emission quantification

We quantify the methane emission rate from the Permian Basin and its spatial distribution with atmospheric inverse modeling, which optimizes spatially-resolved methane emission rates by drawing information from TROPOMI observations and the prior emission estimate following the Bayesian rule. The inversion seeks to optimize monthly methane emission rates resolved at 0.25°× 0.3125° horizontal resolution in a study domain containing the Permian Basin and the surrounding region (29°–34° N, 100°–106° W). The solution to the optimization is found analytically with closed-form characterization of the error statistics (*3*). An atmospheric transport model (a nested version of GEOS-Chem over North America with a 0.25°× 0.3125° horizontal resolution) (*21*) is used as the forward model to relate atmospheric methane columns with ground-level emissions in the study domain and the contributions from outside the domain. The optimization by the inversion significantly reduces the observation-model mismatch with decreased root-mean-square-error (prior: 23 ppbv; posterior: 14 ppbv) and increased correlation (R; prior: 0.30; posterior: 0.62) (fig. S2). See *Methods* for more details about the configurations of the inverse modeling including error accounting and prior information.

When aggregating monthly spatially-resolved posterior emissions to the basin-level annual average, we find a methane emission flux of 2.9±0.5 Tg a^{-1} from the Permian Basin (30–34° N, 101–105° W) (Figure 4A; see *Methods* for the uncertainty analysis). This estimate is more than a factor of two larger than the bottom-up estimate based on an extrapolation of EPA greenhouse gas inventory data (EI_{BU}, 1.2 Tg a^{-1}; see *Methods*) (Figure 4A), suggesting that current methane emissions in the Permian are underrepresented in national bottom-up emission inventories (*22*). Our inversion result is in close agreement with a basin-level estimate based on extrapolation of limited ground-based site-level measurements in the Permian (EI_{ME}, 2.8 Tg a^{-1}) (Figure 4A). It should be noted that these site-level measurements were primarily conducted in the New Mexico portion of the Permian Basin and covered only a small fraction of production sites (see *Methods* and text S2). As a comparison, we also apply a fast mass balance method following Buchwitz et al. (*23*) to estimate basin-level emissions, which yields an annual mean emission rate of 3.2±2.0 Tg a^{-1} for the Permian Basin. This result is consistent with that derived from a full atmospheric inversion. Despite the large uncertainty of the mass balance method, this data-driven approach provides an independent estimate of emissions derived primarily using TROPOMI data (see text S3 for more discussion).

Removing the non-O/G sources (0.2 Tg a^{-1}) from the total flux obtained via the inversion (2.9 Tg a^{-1}), we estimate the methane emissions related to O/G activity to be 2.7 Tg a^{-1} in the Permian Basin. Put in the context of national emissions, this value is approximately one quarter of total emissions from all U.S. oil and gas production areas in 2015 (10.9 Tg a^{-1} including emissions from production, gathering, and processing, which largely occur in the production areas) (*7*). Our estimated emission rate for the Permian is significantly higher than those reported in the literature for other major U.S. O/G producing basins. Table S1 summarizes methane emission estimates for 11 U.S. basins (*7, 24, 25*) from previous aircraft-based studies (i.e., Haynesville (*24,26*), Barnett (*24,27*), Northeast Pennsylvania (*26,28*), Southwest Pennsylvania (*25*), San Juan (*12*), Fayetteville (*26,29*), Bakken (*24,30*), Uinta (*31*), Weld (*32*), West Arkoma (*26*), Eagle Ford (*24*), and the Denver Basin (*24*)). Our estimate for the Permian (2.7 Tg a^{-1}) is about a factor of 4 higher than the largest methane emissions from these previously-reported O/G basins (i.e., Eagle Ford, 0.73 Tg a^{-1}(*24*)), and is even comparable to the 11-basin sum (3.7 Tg a^{-1}) (Figure 4A and table S1). This comparison with recent literature indicates that the Permian Basin is likely the largest observed methane emitting O/G basin in the U.S. and a significant contributor to national O/G related emissions.

Distribution of methane emissions

High-resolution observations from TROPOMI enable us to resolve methane emissions at an unprecedented spatial and temporal resolution, relative to the previous generation of satellite instruments such as GOSAT and SCIAMACHY (*9*). Figure 5 presents the spatial distribution of methane emissions in the Permian Basin at a ~ quarter degree resolution derived from our atmospheric inversion. Compared to the prior inventory EI_{BU}, our inversion finds larger methane emissions near the center of the Delaware and Midland sub-basins. Sensitivity inversions further show that this spatial pattern is robust against prior emissions of varied magnitudes and distributions (fig. S3), demonstrating that it is primarily informed by satellite observations.

The spatial distribution of methane emissions derived from inversion is closely correlated with that of gross gas production (R=0.78), but to a lesser degree with that of oil production (R=0.53) and that of the well number density (R=0.31) (fig. S4). Similarly, when we sum up the O/G-related emissions for two sub-basins, the ratio of methane emissions between Delaware and Midland (1.7 Tg a^{-1}/1.0 Tg a^{-1}=1.7) is closest to the ratio of gas production (1.4), compared to that of oil production (1.0) and well number density (0.7). Because unconventional wells tend to have much higher production per well than conventional wells (*33*), the dependence of methane emissions on gross gas production rather than the well number density suggests that unconventional wells and infrastructure associated with these wells (e.g., gathering stations), which have been developed recently, are likely the major methane emitters in the Permian Basin.

In addition to the spatial distribution, our monthly inversion also provides information about the temporal variation of methane emissions during the 11 months of observation (fig. S5). Although the inversion's ability to resolve the spatial distribution of emissions varies from month to month because of uneven monthly sampling of TROPOMI (fig. S5), our inversion ensemble (table S2 and fig. S5)

generally results in consistent monthly basin-level emission estimates (see also uncertainty analysis in *Methods*). Interestingly, we speculate that high emissions in December 2018 may be related to a very low in-basin gas price towards the end of 2018, resulting from insufficient gas gathering and transmission capacity in the Permian Basin (*33,34*). That said, we do not find an apparent increasing trend in methane emissions, although natural gas production from the Permian Basin increased steadily by ~20% during the overlapping 11-month period (fig. S6). Further investigation is required to delineate factors controlling the temporal variations of O/G-related methane emissions.

Discussion

Using an inverse analysis of TROPOMI satellite observations, we estimate a total methane flux of 2.9±0.5 Tg a^{-1} in the Permian Basin, with 2.7 Tg a^{-1} coming from O/G-related activity. Methane losses of this magnitude represent a waste of an important resource; for instance, this is enough natural gas to supply 7 million households in the state of Texas (*35*). Moreover, the 2.7 Tg a^{-1} methane emitted in Permian results in the same radiative forcing as ~ 260 Tg a^{-1} CO_2 over a 20-year time horizon (86 Tg CO_2 a^{-1} over a 100-year time horizon) (global warming potential of 96 for 20 years and 32 for 100 years) (*7,36*), about the same as annual CO_2 emissions from the entire U.S. residential sector (290 Tg CO_2 a^{-1} in 2017) (*22*).

Our estimate (2.7 Tg a^{-1}) equates to a production-normalized (73 Tg CH_4 a^{-1}, derived from 127 m^3 a^{-1} natural gas production during the study period using 80% methane content by volume) emission rate (or methane leakage rate) of 3.7±0.7%, which is ~ 60% higher than the national average of 2.3±0.3% (*7*) (Figure 4B). The leakage rate is even higher for the rapidly-developing Delaware sub-basin (4.1%). Comparable high leakage rates have also been reported in other oil production focused basins such as the Bakken (*24*) (table S1), but these basins produce much lower natural gas than the Permian Basin does. Previous studies summarized in table S1 show an inverse relationship between the basin-level leakage rate and gas production (*24*); however, the Permian Basin is clearly an outlier with high oil production, high gas production and a high leakage rate.

Overall, the high leakage rate in the Permian Basin appears to be associated with insufficient infrastructure for natural gas gathering, processing, and transportation (*34,37*), leading to extensive venting and flaring (Figure 3), which contributes to high methane emissions. The greater profitability of oil production contributes to a lack of investment in natural gas takeaway capacity, which in turn has resulted in excessive supply of associated gas and a very low in-basin gas price in the Permian (*34*). In addition, with the rescinding of U.S. federal requirements on gas capture and fugitive emissions in 2018, current regulations on O/G methane emissions in the Permian Basin are less stringent at both federal and state levels (see text S4). All these factors may increase the incentive for operators to vent and flare their product. On the other hand, the higher-than-average leakage rate in the Permian Basin implies an opportunity to reduce methane emissions in this rapidly growing oil and gas producing region, through better design, effective management, regulation, and infrastructure development.

Methods

TROPOMI methane observations

We use daily column-averaged dry air column methane mixing ratio (XCH_4) data retrieved from TROPOMI measurements (*38*) between May 2018 and March 2019. TROPOMI, onboard the polar-orbiting Sentinel-5 Precursor satellite, is a push-broom imaging spectrometer that provides near-daily global coverage with a swath width of 2600 km and a nadir ground pixel size of 7×7 km^2 at approximately 13:30 local overpass time (*17*). The retrieval algorithm accounts for the "full physics" of the light path by simultaneously inferring methane concentrations and physical scattering properties, using the Oxygen A-band in the near-infrared (NIR) and the methane absorption band in the short-wave infrared (SWIR) (*39*). Only high-quality XCH_4 measurements retrieved under cloud-free conditions are used in this study (as indicated by the retrieval quality assurance flags in TROPOMI data product). These measurements are filtered for solar zenith angle (<70°), low viewing zenith angle (<60°), smooth topography (1-standard deviation of surface elevation <80 m within 5-km radius), and low aerosol load (aerosol optical thickness <0.3 in NIR) (*40*).

The TROPOMI XCH_4 product is further corrected for any known retrieval biases (*40*). The errors in the TROPOMI XCH_4 measurements have been assessed against GOSAT XCH_4 data (*38*) and were found to correlate with surface albedo. A global bias correction linearly dependent on surface albedo was then derived and applied to the TROPOMI data (*40*). This bias-corrected TROPOMI XCH_4 product is used in this study. Negligible correlation of errors with other retrieved parameters (e.g., aerosol optical thickness) were found in the assessment. Validation with independent ground-based measurements from the Total Column Carbon Observing Network shows that the bias-corrected TROPOMI XCH_4 has a bias of -4.3 ± 7.4 ppbv, improved upon the uncorrected XCH_4 product (-12 ± 11.5 ppbv) (*40*). Additionally, we also examine the correlation between bias-corrected XCH_4 and other retrieved parameters for the subset of TROPOMI data over the domain of this study. We find no correlation with albedo ($R^2 = 0.00$) and a negligible correlation with aerosol optical thickness ($R^2 = 0.07$), supporting that the XCH_4 enhancement over the Permian Basin (Figure 1B) is robust.

Fig. S7A shows the average XCH_4 over the conterminous U.S. and the Permian Basin between May 2018 and March 2019, before the topographical correction. We derive the elevation corrected methane column (XCH_4^t) shown in Figure 1, by applying a 3rd order polynomial correction fitted over the U.S. domain following Kort et al. (*10*). The mass balance method uses the elevation-corrected data (XCH_4^t) for emission quantification, while the inversion method uses XCH_4 (bias corrected) directly obtained from the data product, because the topography effect is taken care of by the atmospheric transport model.

Atmospheric inverse modeling

We perform an inverse analysis of TROPOMI observations to derive optimized estimation of monthly methane emissions at $0.25° \times 0.3125°$ horizontal resolution in the Permian Basin. Quantification of emissions at this combination of relatively high spatial and temporal resolution, not achievable with previous generations of satellite

observations such as from GOSAT or SCIAMACHY, is enabled by higher resolution TROPOMI satellite observations (*41*). Fig. S7B shows that the Permian Basin is well sampled by TROPOMI during the study period, likely because of frequent cloud-free conditions in the region. A total of ~ 200,000 TROPOMI XCH_4 retrievals within the study domain (29°–34°N, 100°–106° W) between May 2018 and March 2019 are used for the inversion.

Let $\boldsymbol{x}$ be the state vector that we seek to optimize through inversion, including a gridded ensemble of methane emissions and an additional element representing the regional model bias in XCH_4. The regional model bias term (a monthly scalar uniform over the inversion domain) is necessary to account for spatially uniform biases caused by imperfect lateral boundary condition and emission errors outside the study domain. The inversion solves for an optimal estimate of $\boldsymbol{x}$ by minimizing the following cost function:

$$J(\boldsymbol{x}) = (\boldsymbol{x} - \boldsymbol{x}_{\mathrm{A}})^T \mathbf{S}_{\mathrm{A}}^{-1} (\boldsymbol{x} - \boldsymbol{x}_A) + (\boldsymbol{y} - \mathbf{K}\boldsymbol{x})^T \mathbf{S}_{\mathrm{O}}^{-1} (\boldsymbol{y} - \mathbf{K}\boldsymbol{x}) \quad (1)$$

where TROPOMI XCH_4 observations are assembled in $\boldsymbol{y}$, $\boldsymbol{x}_{\mathrm{A}}$ is the prior estimate of $\boldsymbol{x}$, $\mathbf{S}_{\mathrm{A}}$ is the prior error covariance matrix, $\mathbf{S}_{\mathrm{O}}$ is the observational error covariance matrix, and $\mathbf{K}$ is the Jacobian matrix describing the sensitivity of XCH_4 to emissions and the regional model bias ($\partial \boldsymbol{y}/\partial \boldsymbol{x}$).

Minimization of Eq. 1 at $\nabla_{\mathrm{x}} J(\boldsymbol{x}) = \mathbf{0}$ yields the posterior estimation ($\hat{\boldsymbol{x}}$), the posterior error covariance matrix ($\hat{\mathbf{S}}$), and the averaging kernel matrix ($\mathbf{A}$): (*42*)

$$\hat{\boldsymbol{x}} = \boldsymbol{x}_{\mathrm{A}} + \mathbf{S}_{\mathrm{A}}\mathbf{K}^T (\mathbf{K}\mathbf{S}_{\mathrm{A}}\mathbf{K}^T + \mathbf{S}_{\mathrm{O}})^{-1} (\boldsymbol{y} - \mathbf{K}\boldsymbol{x}_A) \quad (2)$$

$$\hat{\mathbf{S}} = (\mathbf{K}^T \mathbf{S}_{\mathrm{O}}^{-1} \mathbf{K} + \mathbf{S}_A^{-1})^{-1} \quad (3)$$

$$\mathbf{A} = \mathbf{I}_n - \hat{\mathbf{S}}\mathbf{S}_{\mathrm{A}}^{-1} \quad (4)$$

Here $\mathbf{I}_n$ is an identity matrix where n is the dimension of the state vector $\boldsymbol{x}$. The trace of $\mathbf{A}$, often called as the degrees of freedom for signal (DOFS), quantifies the number of pieces of information constraining the n-dimensional state vector.

To solve for Eq. 2–4, the prior estimate ($\boldsymbol{x}_{\mathrm{A}}$) for gridded methane emissions is required. Using different sources of information, we create two gridded emission inventories for the study region: one based on bottom-up information (EI_{BU}) and the other based on extrapolation of ground-based site-level measurements (EI_{ME}) (see below for descriptions of the inventories). Both emission inventories are time invariant. We use EI_{BU} as the prior estimate in the base inversion, while we use EI_{ME} in a sensitivity inversion to evaluate the impact of the prior estimate (PI_EI_{ME}; see table S2). We perform further evaluations using prior emissions constructed by disaggregating the total O/G-related emission flux from EI_{BU} with varied spatial proxies (i.e. well count, PI_EI_{well}, natural gas production, PI_EI_{gas}, and oil production, PI_EI_{oil}) (table S2 and fig. S3).

The difference between the EI_{BU} and EI_{ME} (Figure 5A and fig. S3A) measures the uncertainty of our prior knowledge, we thus specify prior errors ($\mathbf{S}_{\mathrm{A}}$) for emissions as

the absolute difference between EI_{BU} and EI_{ME}. We also specify the prior error for the regional model XCH_4 bias as 10 ppbv. To test the sensitivity to prior errors, we perturb $\mathbf{S}_A$ in two sensitivity inversions by doubling (PE×2) or halving (PE×0.5) prior errors (table S2). $\mathbf{S}_O$ is constructed with the residual error method (*43*), which results in an error averaged at ~ 11 ppbv. Both $\mathbf{S}_O$ and $\mathbf{S}_A$ are taken to be diagonal matrices. We also perform a sensitivity inversion to test the impact of error correlations with off-diagonal terms specified following Cusworth et al. (*44*) (OE_Cor; see table S2).

A nested version of the GEOS-Chem chemical transport model (12.1.0) is used as the forward model in the inversion to link XCH_4 to surface emissions. To account for the vertical sensitivity of the satellite instrument, we compute simulated XCH_4 by applying TROPOMI averaging kernels to simulated methane vertical profiles. We construct the Jacobian matrix **K**, column by column, with simulations perturbing each state vector element independently. The simulations are performed over North America and adjacent oceans driven by GEOS-FP assimilated meteorological data from the NASA Global Modeling and Assimilation Office (GMAO) on a 0.25°× 0.3125° horizontal grid and 47 vertical layers (~ 30 layers in the troposphere) (*21*). The boundary conditions for the nested-grid simulation are from a 4° × 5° global simulation from May 2018 to March 2019 driven by GEOS-FP meteorological fields. Note that methane emissions and sinks used in this simulation are optimized with previous-year (2010-2017) GOSAT satellite data following Maasakkers et al. (*3*). Such generated boundary conditions may be biased (i.e., unable to capture the growth of global methane concentrations; see fig. S9), and we account for it by introducing a monthly regional model bias term in the inversion. The retrieved regional model biases may vary with the extent of the inversion domain. To test this sensitivity, we also perform an inversion with a larger spatial domain (27°–36°N, 98°–108° W) (Bg_Large; see table S2).

Inversion uncertainty

The posterior error covariance matrix ($\hat{\mathbf{S}}$, Eq. 2) and averaging kernel matrix (**A**, Eq. 3) evaluates the uncertainty of an inversion solution given inversion parameters (e.g., $\mathbf{S}_A$, $\mathbf{S}_O$, forward model). Fig. S5 shows monthly posterior errors for basin-level emissions (derived from $\hat{\mathbf{S}}$) and corresponding degrees-of-freedom for signal (DOFS, trace of **A**) from our base inversion. Overall, the posterior errors for basin-level emissions are < 5% of the estimated emission flux and the DOFS are between 5 and 30 for the monthly inversion, indicating that the TROPOMI data are able to constrain basin-level methane emissions and partially resolve the spatial distribution on a monthly basis. The monthly variations in the posterior error and DOFS are mainly driven by uneven data coverage from TROPOMI sampling. For example, poor data coverage in November 2018 results in a large posterior error and a small DOFS (fig. S5).

We also perform an ensemble of sensitivity inversions by perturbing the configurations and parameters in the base inversion (table S2), aiming to characterize the uncertainties resulting from assumptions made in the inversion not captured by the analytical posterior error. Our results show that all these sensitivity inversions lead to consistent basin-level emission estimates. Annual mean fluxes from sensitivity inversions are within 0.5 Tg a^{-1} of that from our base inversion (table S2), with general agreement in monthly variations as well (fig. S5). Because the

uncertainty resulting from sensitivity inversions are significantly larger than that deduced from posterior error covariance matrix (fig. S5), we report the uncertainty of our basin-level emission estimate (0.5 Tg a^{-1}) as half of the range from the inversion ensemble (2.4 Tg a^{-1} to 3.4 Tg a^{-1}).

Furthermore, to assess the uncertainty due to model transport, we compare hourly GEOS-FP 10m wind speed against measurements at the Midland Airport (MAF) in the Permian Basin during the period of May 2018 and March 2019. Airport wind measurements are not assimilated in the GEOS-FP reanalysis (*45*), so these observations are independent. We find that the GEOS-FP 10m wind speed compares well with the airport measurements in both daytime and nighttime (fig. S8), with mean biases of less than 6% in the mean wind speed. We conclude that errors in the model wind fields are unlikely to be a major source of error in the inversion.

We introduced a regional model bias term in monthly inversions to correct for regional background biases in simulated methane concentrations, which result mainly from imperfect boundary conditions. To check our estimate for this regional bias term, we sample the model simulation to compare with independent observations, i.e., surface measurements at the Mauna Loa Observatory (MLO, a Pacific free tropospheric site upwind of the North American continent) (*46*), tower measurements at Moody, Texas (WKT) (*47*), and aircraft measurements offshore Corpus Christi, Texas (TGC) (*48*). The latter two sites are geographically much closer to the Permian Basin (~ 400 km from WKT and ~ 700 km from TGC) than MLO, but can be affected by local emissions that are not optimized in our inversion. Our results show that the model simulation, when corrected with monthly regional model biases (derived from monthly inversions over the Permian Basin), is able to capture the observed monthly variation in methane concentrations, notably the sharp increase from August to October 2018 in MLO and WKT observations (fig. S9), supporting that it is necessary to optimize the regional model bias in the inversion. Better agreement is observed at MLO and TGC compared to WKT (fig. S9), likely because WKT is located closer to local sources that are not fully optimized in the inversion. Overall, majority of the differences between the prior simulation and TROPOMI observations can be explained by the regional model biases, except for the mismatch in the vicinity of the Permian Basin (fig. S2). We further perform a sensitivity inversion with a varied spatial domain (Bg_Large). Compared to the base inversion, Bg_Large results in a lower regional methane background (by 3 ppbv on average) and a higher methane emission flux (3.4 Tg a^{-1}) (table S2 and fig. S5), reflecting the error correlation between regional methane biases and methane emissions.

In addition, we note that the inversion cannot fully explain the methane enhancement extending outside the Delaware Basin in the northwest direction (near 33°N, 105°W), although the inversion overall substantially improves the agreement between observations and model simulations (fig. S2). While our investigations do not attribute an obvious source of emissions causing the northwestern enhancement (whether oil/gas or other sources), the basin-level O/G emission estimates presented here are robust if this enhancement is caused by non-O/G sources, but are conservative if it is caused by O/G sources.

Emission inventory based on bottom-up information

We create a bottom-up methane emission estimate (EI_{BU}) for the study domain starting from the gridded version of the EPA anthropogenic greenhouse gas emission inventory for 2012 (*49*). Maasakkers et al. *(49*) developed a procedure to spatially and temporally allocate the national sectorial methane emissions reported in the U.S. Inventory of Greenhouse Gas Emissions and Sinks (GHGI) by U.S. EPA on a 0.1° × 0.1° grid, using various databases at the state, county, local, and point source level. The emission inventory includes methane emissions from agriculture, coal mining, natural gas systems, petroleum (oil) systems, waste, and other minor anthropogenic sources.

To reflect the intensifying exploitation activity in recent years in the Permian Basin, we then make an extrapolation of the methane emissions from the oil and gas production sector, using 2018 Enverus Drillinginfo data on well count, well completion, and production (*50*). We further scale the sub-sectorial production emissions using the ratio between the latest GHGI (*22*) and the GHGI that Maasakkers et al. (*49*) was based on (*51*) for 2013 emissions, to account for the changes in the national average emission factors. The updates result in total methane emissions of 1.2 Tg a^{-1} in the Permian Basin (blue box in Figure 5A), with 1.0 Tg a^{-1} coming from O/G-related emissions and the remainder mainly from agriculture. We use this updated gridded emission inventory (EI_{BU}) as the prior emission estimate for the inversion. The resulting emissions inventory dataset (EI_{BU} inventory) is publicly available for our study region encompassing the entire Permian Basin (https://doi.org/10.7910/DVN/HH4EUM).

Emission inventory based on site-level emission measurements

An alternative prior estimation of methane emissions is obtained by extrapolating ground-based methane emission measurements from a limited sample of oil and gas production sites in the Permian Basin (primarily in the New Mexico portion of the basin) during July and August 2018 (*52*). The measurements found a wide range of site-level emission rates, which appear to be associated with the complexity of infrastructure, and were classified into emission rates for simple (with only wellheads and/or pump jacks) vs. complex sites (also with storage tanks and/or compressors). Extrapolating these site-level emission rates to the entire Permian gave a basin-level methane emission rate of 2.3 Tg $a^{-1}$from O/G production. Additional emissions from compressor stations and processing plants are estimated to be 0.22 Tg a^{-1} and 0.14 Tg a^{-1}, respectively, using activity data from Enverus Drillinginfo's midstream infrastructure dataset, facility-level emission factors from literature (*53, 54*), and blowdown event emission factors from GHGI (*22*). We then disaggregate the basin-level O/G-related emissions to a 0.1° × 0.1° grid by the spatial distribution of gas production (Figure 2D). To complete the inventory, non-O/G anthropogenic methane emissions (0.2 Tg a^{-1}) are taken from EI_{BU}. This emission inventory (EI_{ME}), based primarily on extrapolation of limited site-level measurements, provides an alternative prior estimate for the inversion and is used to test the sensitivity of the results to the choice of prior information (fig. S3). See text S2 for detailed information regarding the site-level measurements and the extrapolation procedure. See text S2 for detailed information regarding the site-level measurements and the extrapolation procedure. The resulting emissions inventory dataset (EI_{ME} inventory) is publicly available for

our study region encompassing the entire Permian Basin (https://doi.org/10.7910/DVN/HH4EUM).

H2: Supplementary Materials

Text S1. Methods for estimating gas flaring volume
Text S2. Site-level emission measurements and extrapolation to the basin
Text S3. Mass balance method for emission quantification
Text S4. Current status of regulation in the Permian Basin
Fig. S1. Annual mean gas flaring radiant heat over the Permian Basin observed by VIIRS from 2012 to 2018
Fig. S2. Observed and simulated XCH_4 over the Permian Basin.
Fig. S3. Spatial distribution of methane emission rates in the Permian Basin in alternative prior emission inventories and the corresponding posterior estimates.
Fig. S4. Spatial correlation between the posterior methane emission rates and O/G production activities for each grid cell.
Fig. S5. Monthly methane emission rates estimated by the base and sensitivity inversions and analytical posterior error.
Fig. S6. Monthly natural gas production and gas price in the Permian Basin.
Fig. S7. TROPOMI XCH4 observations over the conterminous U.S.
Fig. S8. Evaluation of GEOS-FP wind speed in daytime and nighttime.
Fig. S9. Regional model biases inferred from the TROPOMI inversion and evaluation with independent observations.
Table S1. Estimates of O/G-related methane emissions reported in previous aircraft-based studies for 11 U.S. O/G producing basins.
Table S2. Total basin-level methane emission estimates from an ensemble of sensitivity inversions perturbing a variety of inversion parameters.

References and Notes

1. D. Shindell, J. C. I. Kuylenstierna, E. Vignati, R. van Dingenen, M. Amann, Z. Klimont, S. C. Anenberg, N. Muller, G. Janssens-Maenhout, F. Raes, J. Schwartz, G. Faluvegi, L. Pozzoli, K. Kupiainen, L. Höglund-Isaksson, L. Emberson, D. Streets, V. Ramanathan, K. Hicks, N. T. K. Oanh, G. Milly, M. Williams, V. Demkine, D. Fowler, Simultaneously Mitigating Near-Term Climate Change and Improving Human Health and Food Security. *Science* **335**, 183-189 (2012).
2. G. Myhre *et al.*, in *Climate Change 2013: The Physical Science Basis. Contribution of Working Group I to the Fifth Assessment Report of the Intergovernmental Panel on Climate Change,* T. F. Stocker *et al.*, Eds. (Cambridge University Press, Cambridge, UK, 2013), pp. 659-740.
3. J. D. Maasakkers *et al.*, Global distribution of methane emissions, emission trends, and OH concentrations and trends inferred from an inversion of GOSAT satellite data for 2010–2015. *Atmos. Chem. Phys.* **19**, 7859-7881 (2019).
4. S. Schwietzke, O. A. Sherwood, L. M. P. Bruhwiler, J. B. Miller, G. Etiope, E. J. Dlugokencky, S. E. Michel, V. A. Arling, B. H. Vaughn, J. W. C. White, P. P. Tans, Upward revision of global fossil fuel methane emissions based on isotope database. *Nature* **538**, 88-91 (2016).

5. B. Hmiel, V. V. Petrenko, M. N. Dyonisius, C. Buizert, A. M. Smith, P. F. Place, C. Harth, R. Beaudette, Q. Hua, B. Yang, I. Vimont, S. E. Michel, J. P. Severinghaus, D. Etheridge, T. Bromley, J. Schmitt, X. Faïn, R. F. Weiss, E. Dlugokencky, Preindustrial $^{14}CH_4$ indicates greater anthropogenic fossil CH_4 emissions. *Nature* **578**, 409-412 (2020).

6. R. A. Alvarez, S. W. Pacala, J. J. Winebrake, W. L. Chameides, S. P. Hamburg, Greater focus needed on methane leakage from natural gas infrastructure. *Proceedings of the National Academy of Sciences* **109**, 6435-6440 (2012).

7. R. A. Alvarez *et al.*, Assessment of methane emissions from the U.S. oil and gas supply chain. *Science* **361**, 186-188 (2018).

8. EPA. Inventory of US Greenhouse Gas Emissions and Sinks: 1990−2015. https://www.epa.gov/ghgemissions/inventory-us-greenhouse-gas-emissions-and-sinks-1990-2015 (2017).

9. D. J. Jacob *et al.*, Satellite observations of atmospheric methane and their value for quantifying methane emissions. *Atmos. Chem. Phys.* **16**, 14371-14396 (2016).

10. E. A. Kort *et al.*, Four corners: The largest US methane anomaly viewed from space. *Geophysical Research Letters* **41**, 6898-6903 (2014).

11. C. Frankenberg *et al.*, Airborne methane remote measurements reveal heavy-tail flux distribution in Four Corners region. *Proceedings of the National Academy of Sciences* **113**, 9734-9739 (2016).

12. M. L. Smith *et al.*, Airborne Quantification of Methane Emissions over the Four Corners Region. *Environmental Science & Technology* **51**, 5832-5837 (2017).

13. EIA. Drilling Productivity Report. https://www.eia.gov/petroleum/drilling/, Accessed on May 1, 2019 (2019).

14. C. Krauss, The 'Monster' Texas Oil Field That Made the U.S. a Star in the World Market, in *The New York Times*. (2019).

15. K. A. Willyard, G. W. Schade, Flaring in two Texas shale areas: Comparison of bottom-up with top-down volume estimates for 2012 to 2015. *Science of The Total Environment* **691**, 243-251 (2019).

16. SRON, "S5P Mission Performance Centre Methane [L2__CH4___] Readme, S5P-MPC-SRON-PRF-CH4, V01.03.02," (2019).

17. J. P. Veefkind *et al.*, TROPOMI on the ESA Sentinel-5 Precursor: A GMES mission for global observations of the atmospheric composition for climate, air quality and ozone layer applications. *Remote Sensing of Environment* **120**, 70-83 (2012).

18. EIA. The Wolfcamp play has been key to Permian Basin oil and natural gas production growth. https://www.eia.gov/todayinenergy/detail.php?id=37532#tab1, Accessed on Aug 18, 2019 (2018).

19. Y. Zhang *et al.*, Satellite-Observed Changes in Mexico's Offshore Gas Flaring Activity Linked to Oil/Gas Regulations. *Geophysical Research Letters* **46**, 1879-1888 (2019).

20. B. N. Duncan *et al.*, A space-based, high-resolution view of notable changes in urban NOx pollution around the world (2005–2014). *Journal of Geophysical Research: Atmospheres* **121**, 976-996 (2016).

21. J. X. Sheng *et al.*, High-resolution inversion of methane emissions in the Southeast US using SEAC4RS aircraft observations of atmospheric methane: anthropogenic and wetland sources. *Atmos. Chem. Phys.* **18**, 6483-6491 (2018).

22. EPA. Inventory of US Greenhouse Gas Emissions and Sinks: 1990−2017. https://www.epa.gov/ghgemissions/inventory-us-greenhouse-gas-emissions-and-sinks-1990-2017 (2019).

23. M. Buchwitz *et al.*, Satellite-derived methane hotspot emission estimates using a fast data-driven method. *Atmos. Chem. Phys.* **17**, 5751-5774 (2017).

24. J. Peischl *et al.*, Quantifying Methane and Ethane Emissions to the Atmosphere from Central and Western U.S. Oil and Natural Gas Production Regions. *Journal of Geophysical Research: Atmospheres* **123**, 7725-7740 (2018).

25. X. Ren, D. L. Hall, T. Vinciguerra, S. E. Benish, P. R. Stratton, D. Ahn, J. R. Hansford, M. D. Cohen, S. Sahu, H. He, C. Grimes, J. D. Fuentes, P. B. Shepson, R. J. Salawitch, S. H. Ehrman, R. R. Dickerson, Methane Emissions from the Marcellus Shale in Southwestern Pennsylvania and Northern West Virginia Based on Airborne Measurements. *Journal of Geophysical Research: Atmospheres* **124**, 1862-1878 (2019).

26. J. Peischl *et al.*, Quantifying atmospheric methane emissions from the Haynesville, Fayetteville, and northeastern Marcellus shale gas production regions. *Journal of Geophysical Research: Atmospheres* **120**, 2119-2139 (2015).

27. A. Karion *et al.*, Aircraft-Based Estimate of Total Methane Emissions from the Barnett Shale Region. *Environmental Science & Technology* **49**, 8124-8131 (2015).

28. Z. R. Barkley *et al.*, Quantifying methane emissions from natural gas production in north-eastern Pennsylvania. *Atmos. Chem. Phys.* **17**, 13941-13966 (2017).

29. S. Schwietzke *et al.*, Improved Mechanistic Understanding of Natural Gas Methane Emissions from Spatially Resolved Aircraft Measurements. *Environmental Science & Technology* **51**, 7286-7294 (2017).

30. J. Peischl *et al.*, Quantifying atmospheric methane emissions from oil and natural gas production in the Bakken shale region of North Dakota. *Journal of Geophysical Research: Atmospheres* **121**, 6101-6111 (2016).

31. A. Karion *et al.*, Methane emissions estimate from airborne measurements over a western United States natural gas field. *Geophysical Research Letters* **40**, 4393-4397 (2013).

32. G. Pétron *et al.*, A new look at methane and nonmethane hydrocarbon emissions from oil and natural gas operations in the Colorado Denver-Julesburg Basin. *Journal of Geophysical Research: Atmospheres* **119**, 6836-6852 (2014).

33. M. Omara *et al.*, Methane Emissions from Conventional and Unconventional Natural Gas Production Sites in the Marcellus Shale Basin. *Environmental Science & Technology* **50**, 2099-2107 (2016).

34. RBN Energy, "Hell In Texas - Permian Gas Takeaway Headed For Capacity Wall," *RBN Energy Drill Down Report* (2018).
35. EIA. Natural Gas Consumption by End Use. https://www.eia.gov/dnav/ng/ng_cons_sum_dcu_STX_a.htm. Accessed on Aug 20, 2019 (2019).
36. M. Etminan, G. Myhre, E. J. Highwood, K. P. Shine, Radiative forcing of carbon dioxide, methane, and nitrous oxide: A significant revision of the methane radiative forcing. *Geophysical Research Letters* **43**, 12,614-612,623 (2016).
37. T. Curtis, B. Montalbano, "The Permian Basin Produces Gas, Too —Permian Basin Oil and Gas Production Growth: A Case Study for Gas Infrastructure Needs in the U.S.," (Energy Policy Research Foundation, Inc., 2018).
38. H. Hu *et al.*, Toward global mapping of methane with TROPOMI: first results and intersatellite comparison to GOSAT. *Geophys. Res. Lett.* **45**, (2018).
39. H. Hu *et al.*, The operational methane retrieval algorithm for TROPOMI. *Atmos. Meas. Tech.* **9**, 5423-5440 (2016).
40. O. Hasekamp *et al.*, "Algorithm Theoretical Baseline Document for Sentinel-5 Precursor methane retrieval (issue 1.10), SRON-S5P-LEV2-RP-001," (SRON, 2019).
41. J. X. Sheng, D. J. Jacob, J. D. Maasakkers, Y. Zhang, M. P. Sulprizio, Comparative analysis of low-Earth orbit (TROPOMI) and geostationary (GeoCARB, GEO-CAPE) satellite instruments for constraining methane emissions on fine regional scales: application to the Southeast US. *Atmos. Meas. Tech.* **11**, 6379-6388 (2018).
42. G. P. Brasseur, D. J. Jacob, *Modeling of Atmospheric Chemistry*. (Cambridge University Press, Cambridge, 2017).
43. C. L. Heald *et al.*, Comparative inverse analysis of satellite (MOPITT) and aircraft (TRACE-P) observations to estimate Asian sources of carbon monoxide. *Journal of Geophysical Research: Atmospheres* **109**, D23306 (2004).
44. D. H. Cusworth, D. J. Jacob, J. X. Sheng, J. Benmergui, A. J. Turner, J. Brandman, L. White, C. A. Randles, Detecting high-emitting methane sources in oil/gas fields using satellite observations. *Atmos. Chem. Phys.* **18**, 16885-16896 (2018).
45. Rienecker, M. M., et al. (2008). The GEOS-5 Data Assim- ilation System—Documentation of versions 5.0.1, 5.1.0, and 5.2.0. NASA Tech. Rep. NASA/TM-2008-104606, Vol. 27, 118 pp., https://gmao.gsfc.nasa.gov/pubs/docs/Rienecker369.pdf
46. E.J. Dlugokencky, A.M. Crotwell, P.M. Lang, J.W. Mund, M.E. Rhodes, Atmospheric Methane Dry Air Mole Fractions from quasi-continuous measurements at Barrow, Alaska and Mauna Loa, Hawaii, 1986-2017, Version: 2019-06-21, Path: ftp://aftp.cmdl.noaa.gov/data/trace_gases/ch4/in-situ/surface/ (2018)
47. A. E. Andrews, J. D. Kofler, M. E. Trudeau, J. C. Williams, D. H. Neff, K. A. Masarie, D. Y. Chao, D. R. Kitzis, P. C. Novelli, C. L. Zhao, E. J. Dlugokencky, P. M. Lang, M. J. Crotwell, M. L. Fischer, M. J. Parker, J. T. Lee, D. D. Baumann, A. R. Desai, C. O. Stanier, S. F. J. De Wekker, D. E. Wolfe, J. W. Munger, P. P. Tans, CO_2, CO, and CH_4 measurements from tall towers in the

NOAA Earth System Research Laboratory's Global Greenhouse Gas Reference Network: instrumentation, uncertainty analysis, and recommendations for future high-accuracy greenhouse gas monitoring efforts. *Atmos. Meas. Tech.* **7**, 647-687 (2014).

48. C. Sweeney, A. Karion, S. Wolter, T. Newberger, D. Guenther, J. A. Higgs, A. E. Andrews, P. M. Lang, D. Neff, E. Dlugokencky, J. B. Miller, S. A. Montzka, B. R. Miller, K. A. Masarie, S. C. Biraud, P. C. Novelli, M. Crotwell, A. M. Crotwell, K. Thoning, P. P. Tans, Seasonal climatology of CO_2 across North America from aircraft measurements in the NOAA/ESRL Global Greenhouse Gas Reference Network. *Journal of Geophysical Research: Atmospheres* **120**, 5155-5190 (2015).

49. J. D. Maasakkers *et al.*, Gridded National Inventory of U.S. Methane Emissions. *Environmental Science & Technology* **50**, 13123-13133 (2016).

50. Enverus DrillingInfo. DI Desktop. didesktop.com (2019).

51. EPA. Inventory of US Greenhouse Gas Emissions and Sinks: 1990−2014. https://www.epa.gov/ghgemissions/inventory-us-greenhouse-gas-emissions-and-sinks-1990-2014 (2016).

52. EDF. New Mexico Oil & Gas Data. https://www.edf.org/nm-oil-gas/, Accessed on Aug 18, 2019 (2019)

53. A. J. Marchese *et al.*, Methane Emissions from United States Natural Gas Gathering and Processing. *Environmental Science & Technology* **49**, 10718-10727 (2015).

54. A. L. Mitchell *et al.*, Measurements of Methane Emissions from Natural Gas Gathering Facilities and Processing Plants: Measurement Results. *Environmental Science & Technology* **49**, 3219-3227 (2015).

55. C. Elvidge, M. Zhizhin, K. Baugh, F.-C. Hsu, T. Ghosh, Methods for Global Survey of Natural Gas Flaring from Visible Infrared Imaging Radiometer Suite Data. Energies 9, 14 (2016).

56. A. M. Robertson *et al.*, Variation in Methane Emission Rates from Well Pads in Four Oil and Gas Basins with Contrasting Production Volumes and Compositions. *Environmental Science & Technology* **51**, 8832-8840 (2017).

57. D. Zavala-Araiza, D. R. Lyon, R. A. Alvarez, K. J. Davis, R. Harriss, S. C. Herndon, A. Karion, E. A. Kort, B. K. Lamb, X. Lan, A. J. Marchese, S. W. Pacala, A. L. Robinson, P. B. Shepson, C. Sweeney, R. Talbot, A. Townsend-Small, T. I. Yacovitch, D. J. Zimmerle, S. P. Hamburg, Reconciling divergent estimates of oil and gas methane emissions. *Proceedings of the National Academy of Sciences* **112**, 15597-15602 (2015).

Acknowledgments

General: This work was partially supported by the Kravis Scientific Research Fund at Environmental Defense Fund (EDF). Y.Z. was funded by the Kravis Fellowship through EDF and by Harvard University. The authors thank the team that realized the TROPOMI instrument and its data products, consisting of the partnership between Airbus Defense and Space Netherlands, KNMI, SRON, and TNO, commissioned by NSO and ESA. Sentinel-5 Precursor is part of the EU Copernicus program, and

Copernicus Sentinel data 2018-2019 has been used. The authors acknowledge the provision of publicly available VIIRS night-fire data. The authors also acknowledge NOAA Earth System Research Laboratory's Global Greenhouse Gas Reference Network for providing methane measurements at MLO, WKT, and TGC. P.S. and S.P. are funded through the GALES project (#15597) by the Dutch Technology Foundation STW, which is part of the Netherlands Organization for Scientific Research (NWO). A.L. acknowledges funding from the TROPOMI national program through NSO. R.G., M.O., D.L., D.Z.-A., R.A.A. and S.P.H. were funded by the Robertson Foundation.

Funding: Kravis Scientific Research Fund, the Robertson Foundation, GALES project (#15597) by the Dutch Technology Foundation STW, and the TROPOMI national program NSO.

Author contributions: Y.Z. and R.G. led the study and wrote the manuscript with inputs from all coauthors; Y.Z. performed inversion simulations, carried out sensitivity experiments, and interpreted results with inputs from D.J.J.; S.P., P.S., S.H., A.L.D, I.A. analyzed TROPOMI data and provided mass balance calculations; J.D.M. provided bottom-up inventory data analysis; M.O., D.L., D.Z.A., R.A., S.P.H. provided field-measurement-based inventory data analysis; H.O.N, M.P.S. contributed to setting up the nested GEOS-Chem simulation; D.J.V. evaluated GEOS-FP wind data; Y.Z., R.Z. analyzed VIIRS radiant heat and TROPOMI NO_2 data; All authors provided scientific inputs during the analysis, and reviewed and commented on the manuscript.

Competing interests: The authors declare that they have no competing interests.

Data and materials availability: Spatially resolved methane emission estimates over the Permian Basin from this study (EI_{BU}, EI_{ME}, and the posterior estimate from atmospheric inverse modeling) can be accessed through https://doi.org/10.7910/DVN/HH4EUM.TROPOMI data are available through https://scihub.copernicus.eu/. VIIRS radiant heat data available through https://eogdata.mines.edu/download_viirs_fire.html. The GEOS-Chem model is available at https://doi.org/10.5281/zenodo.1553349

Figures and Tables

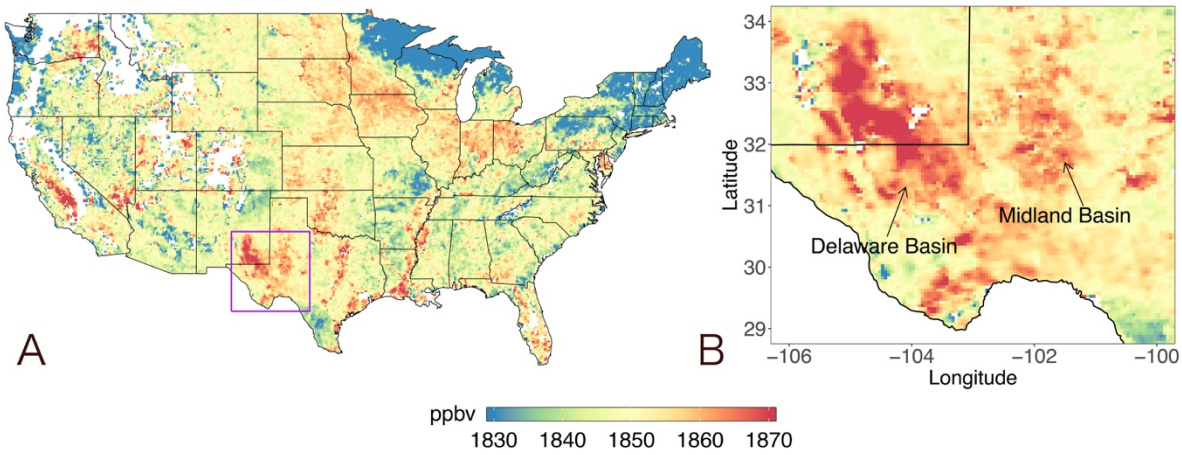

Fig. 1. TROPOMI satellite data derived elevation-corrected column methane mixing ratio for (A) the conterminous U.S. and (B) the Permian Basin containing the Delaware and the Midland sub-basins. White shading represents missing data. Purple boundary in A indicates the study domain encompassing the Permian Basin. Methane averages are computed from monthly means of TROPOMI measurements during May 2018 and March 2019.

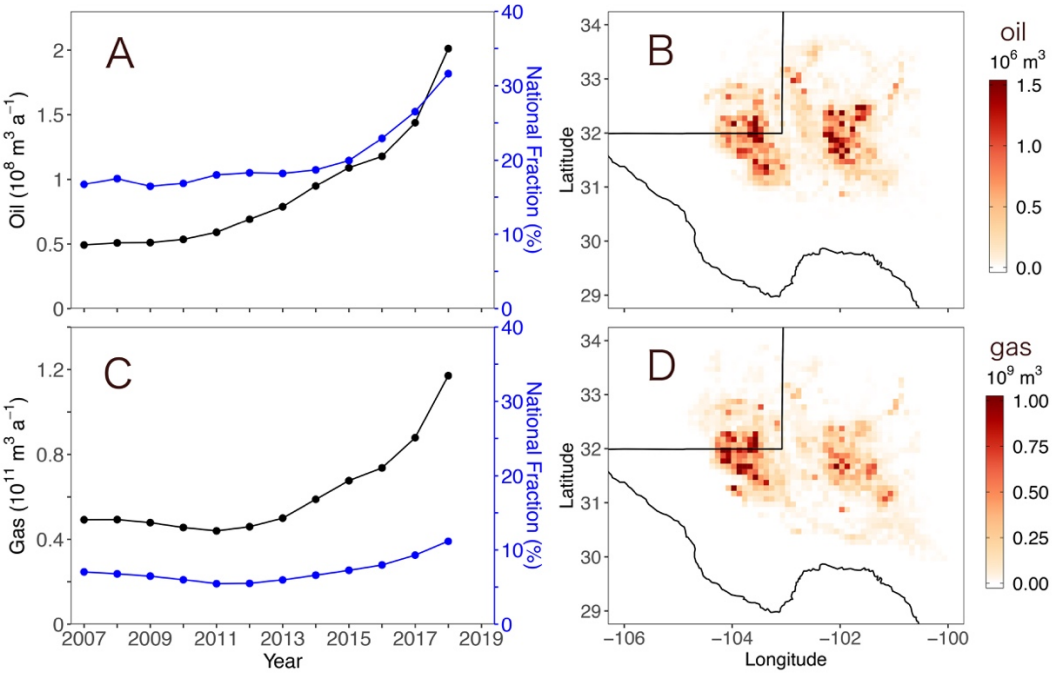

Fig. 2. Oil and gas production in the Permian Basin. A and C show time series of annual oil and natural gas production in black and the corresponding fractions of total U.S. production in blue (data from the Drilling Productivity Report by EIA (*13*)). B and D show the spatial distribution of oil and gas production for 2018 (data from Enverus Drillinginfo (*50*)). Oil production includes both crude and condensate production. Gas production represents gross (before processing) gas production.

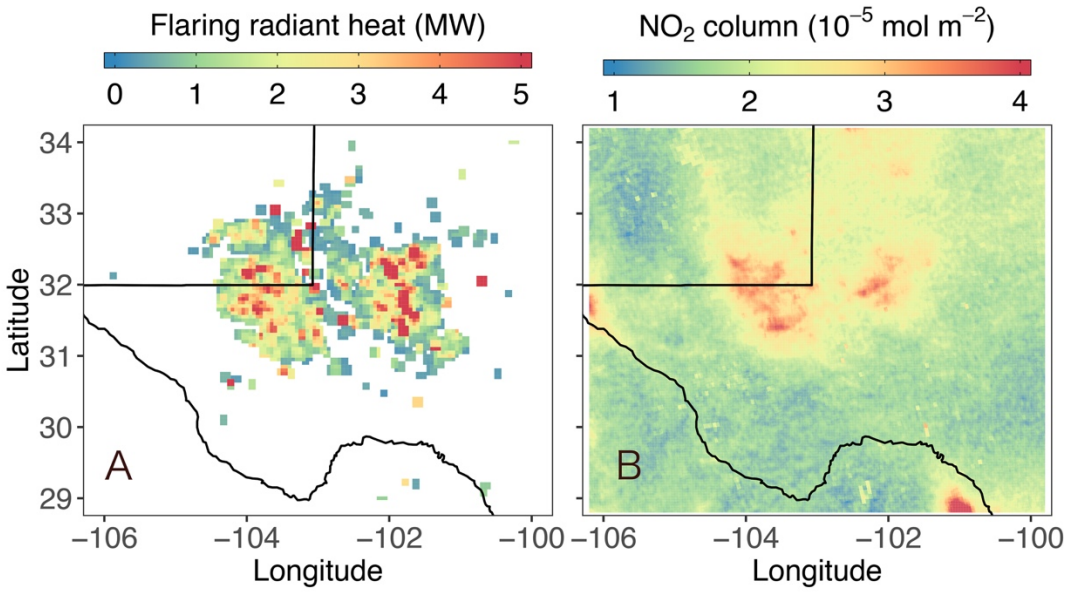

Fig. 3. Satellite observations of (A) gas flaring radiant heat and (B) NO_2 tropospheric column density over the Permian Basin. The flaring radiant heat is the annual average of 2018 measured by the VIIRS satellite instrument, and NO_2 tropospheric column density is the 3-month average (June, July, and August of 2018) measured by the TROPOMI instrument, indicating co-located hotspots over the Delaware and Midland sub-basins.

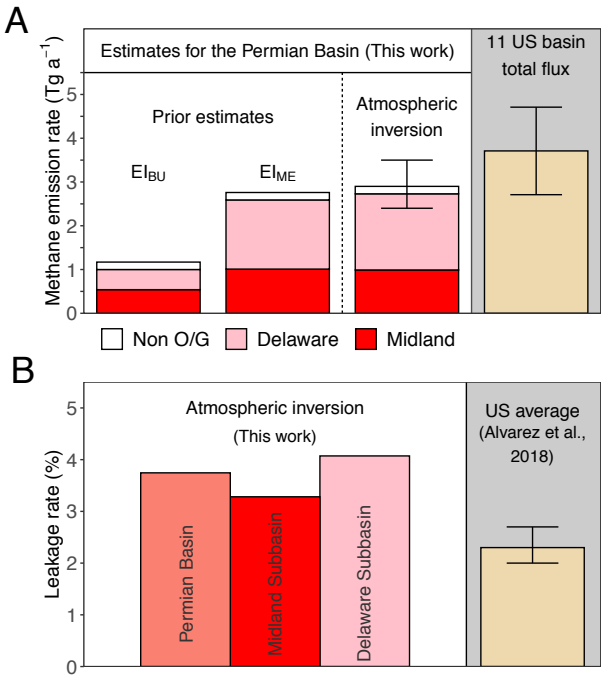

Fig. 4. Methane emission quantification for the Permian Basin. (A) Annual methane emissions from the Permian Basin from two prior emission inventories (EI_{BU} and EI_{ME}), and TROPOMI satellite data based atmospheric inversion and a mass balance method. The break-down for Delaware, Midland, and non-O/G sources are shown in pink, red, and white for EI_{BU}, EI_{ME}, and atmospheric inversion. The estimate for the Permian Basin is compared with total emissions from 11 U.S. basins reported in literature (*7, 24, 25*) (table S1). (B) Leakage rates for the Permian Basin and two sub-basins, in comparison with the average leakage reported for the entire U.S. (*7*)

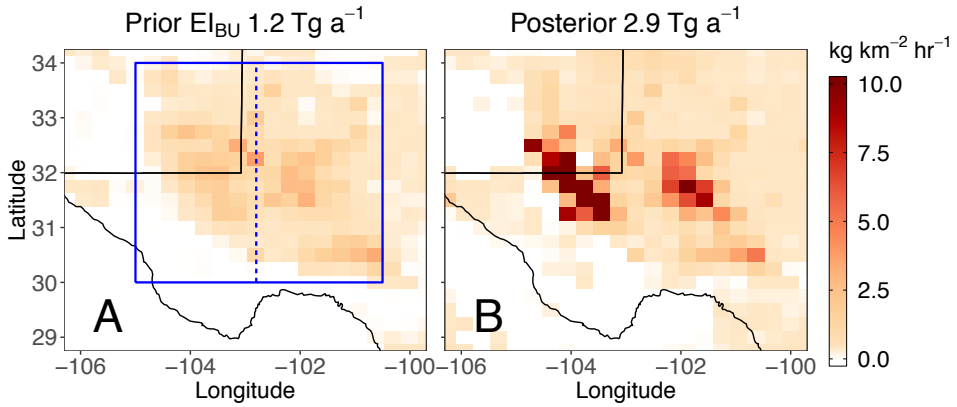

Fig. 5. Spatial distribution of methane emission rates in the Permian Basin. (A) Bottom-up emission inventory EI_{BU} extrapolated from EPA greenhouse gas inventory data (prior). (B) TROPOMI observation derived emissions using Bayesian atmospheric inverse modeling (posterior). The prior and posterior basin-total emissions, indicated on top of the figure, are computed over the area enclosed by the solid blue boundary, with contributions from two sub-basins, the Delaware (left of the dashed line) and Midland (right of the dashed line).

Supplementary Materials

Supplementary Text

Text S1: Methods for estimating gas flaring volume

We use the nighttime fire and flare data observed by the Visible Infrared Imaging Radiometer Suite (VIIRS) instrument onboard the Suomi National Polar-Orbiting Partnership satellite to support our analysis (https://eogdata.mines.edu/download_viirs_fire.html; data access: August 1, 2019). The product Nightfire V2.1 (CLASS) is available for the period from 2012 to 2017, while the product Nightfire V3.1 (GRAVITE) is available for the period starting 2018. We select the data with retrieved flame temperature between 1400–2500 K within the study domain. Combustion in this temperature range is usually associated with gas flaring. The spatial distribution of the flaring radiant heat in Permian is presented in Figure 3 and the evolution of the flaring radiant heat is presented in fig. S1.

We also estimate the gas flaring volume in Permian between May 2018 and March 2019 following an empirical relationship with the radiant heat proposed by Elvidge et al. (*55*):

$$V = 0.0274\, H^{0.7}$$

where H is the VIIRS observed radiant heat in MW and V is the gas flaring rate in 10^9 m^3 a^{-1}. The average and the standard deviation of the flaring rate during the study period is computed with daily basin-level flaring rates aggregated from individual detected flares. We estimate a flaring rate of 5.9±1.2 billion m^3 a^{-1} during May 2018 and March 2019. In comparison, the operator self-reported venting and flaring in the Permian Basin is 4.5 billion m^3 a^{-1} for 2018, according to the New Mexico Oil Conservation Division (www.emnrd.state.nm.us/OCD/statistics.html) and the Texas Railroad Commission (www.rrc.state.tx.us/oil-gas/research-and-statistics/production-data/). Previous assessments show that operator self-reported flaring data are consistently lower than satellite-based observations (*15*).

We can further compute the mass of methane contained in the flared gas (M) as

$$M = m_{\mathrm{CH_4}} \gamma \frac{V}{\upsilon}$$

where υ is 0.0224 m^3 mol^{-1} under STP conditions, m_{CH4} is 16 g mol^{-1}, and γ is the fraction of methane in natural gas (~ 80% for the Permian Basin according to EPA Oil and Gas Emissions Estimation Tool Version 1.5). Methane emissions from gas flaring can then be computed as $(1-\epsilon)M$, and methane converted to CO_2 during flaring as ϵM, where ϵ is the flaring combustion efficiency. We thus estimate that 3.4±0.8 methane Tg a^{-1} is sent to flaring. Assuming a flaring efficiency between 95%-98%, this indicates direct methane emissions of 0.07-0.17 Tg a^{-1} from gas flaring, less than 6% of the total methane emission estimate based on TROPOMI data. 3.2-3.3 Tg a^{-1} methane is converted to CO_2 during flaring.

As a form of background information, there are 154,540 active wells with 6,555 new wells (< 1 year old) in the Permian Basin during the study period (May 2018 – March 2019), according to Enverus Drillinginfo (*50*). Here, active wells are defined as wells that either reported their oil/gas production for at least six months during the study period or reported non-zero oil/gas production at the end of the study period (March

2019). While information regarding permits in the New Mexico portion of the Permian Basin is unavailable, we estimate a total of 3,364 venting and flaring permits are effective for the Texas portion of the basin during the study period, based on the data from the Texas Railroad Commission.

Text S2: Site-level emission measurements and extrapolation to the Permian Basin

We provide here details of recent ground-based measurements and their extrapolation that were used to construct an alternative measurement-based bottom-up inventory for the Permian Basin, as an input to the atmospheric inversion modeling. The methodology and results were made publicly available in April 2019 via Environmental Defense Fund's New Mexico oil and gas pollution study (*52*). The resulting emission inventory dataset (EI_{ME} inventory) is publicly available for our study region encompassing the entire Permian Basin (DOI: 10.7910/DVN/HH4EUM).

Here, we provide a summary of the measurements, methodology and results. Ground-based site-level methane emission measurements at 93 oil and gas production sites in the Permian Basin were performed in July and August 2018 with a stationary downwind plume measurement technique (OTM-33A) (*52*), in which methane concentration measurements were taken downwind of target sites at 0.5 Hz using a Picarro cavity-ring down spectrometer (Model G2204). OTM-33A is a well-established emission rate quantification method that utilizes stationary downwind measurements coupled with Gaussian plume dispersion modeling to estimate site-level methane leak rates. Previous controlled release tests indicated a 95% confidence interval of +/-56% on mean site-level emissions quantified using the OTM-33A methodology (with a -10% bias) (*56*).

The sampling was carried out predominantly in the New Mexico portion of the Permian Basin, following a stratified random sampling approach to account for the wide diversity of well age within the oil producing fields. Final site selection at a particular field was determined by local meteorology on the day of measurements as well as access to public roads downwind of target sites. A FLIR optical gas-imaging camera is used to identify major emission sources such as storage tanks and to facilitate positioning of the vehicle within the plume.

In this study, sites were recorded as below the detection limit (BDL) if no clear plume was detected downwind. The BDL was estimated at 0.04 kg/h based on previous work (*56*). In total, 52 sites were reported to have BDL emissions while 41 sites had emissions that were above the detection limit. The detectability of emissions from a site are found to be closely associated with the complexity of infrastructure. Emissions were below the detection limit (0.04 kg/h/site) for over 90% of "simple" sites (with only wellheads and/or pump jacks), but were detectable for most (78%) "complex" sites (also with storage tanks and/or compressors). We determine the site-level emission factor for "simple" sites to be 0.04 kg/h/site and that for "complex" sites to be 5.2 kg/h/site. For the latter, a lower bound estimate following the procedure described in Zavala-Araiza et al. (*57*) (5.2–79 kg CH_4/h/site) is used here for a conservatively low estimate.

To extrapolate to basin-level emissions based on the above measurements, we need to estimate the number of "simple" vs. "complex" sites in Permian. We used satellite imagery data from Google Maps to perform manual classification ("simple", "complex", or "unknown") of 25,000 well sites in the New Mexico portion of the Delaware Basin. Human classification of well site images was achieved via a crowdsourcing marketplace—Amazon Mechanical Turk (https://www.mturk.com/). Depending on the observed equipment on site, each image representing a well site

location was manually classified by five workers as either a “simple” site, a “complex” site, or a site of “unknown” configuration. A site’s final classification was determined based on at least a 60% agreement among the workers. On average, 33% of the sites were classified as “complex” sites and 58% were classified as “simple” sites, with the remainder (8.6%) being sites of “unknown” configuration. We assume this distribution for the New Mexico portion of the Delaware Basin applies to the whole Permian Basin and count the “unknown” category as “simple”. We therefore estimate that the numbers for “simple” and “complex” sites are 97,000 and 48,600, respectively. Combining site classifications with corresponding site-level emission factors leads to an estimate of 2.3 Tg a^{-1} for methane emissions from O/G production in the Permian Basin.

Text S3 Mass balance method for emission quantification

As an independent comparison of our inverse modeling results, we apply the mass balance method of Buchwitz et al. (*23*) to derive the average methane emission rate over the Permian Basin (30-34 °N, 101-105 °W). This data-driven approach does not require prior emissions and atmospheric transport model, and therefore is a fast algorithm, compared to atmospheric inversion. With large amount of high resolution observations delivered by satellite instruments such as TROPOMI, the method has potential as a quick screening and assessment tool for quantifying regional annual methane emissions.

Here, we apply the method to the elevation corrected methane column XCH_4^t data from May 2018 – March 2019 regridded to 0.2° × 0.2° (Figure 1). The emission rate (Q, Tg yr^{-1}) is computed by applying a conversion factor (CF) to the XCH_4^t enhancement (ΔXCH_4^t, ppbv, computed as mean XCH_4^t in the source region minus mean XCH_4^t in the surrounding background) as follows (*23*):

$$Q = \Delta XCH_4^t \times CF$$
$$CF = L \times V \times M_{exp} \times M \times C$$

where L is the effective length of the source area (computed as square root of the source area, 375 km) through which wind of effective speed V (17 km hr^{-1}) ventilates the air parcel carrying emitted methane, M_{exp} is the ratio of average surface pressure in the region (898.32 hPa for Permian) and standard surface pressure of 1013.25 hPa, M is a constant to convert mole fraction to mass change per area (5.345 kg CH_4 km^{-2} ppb^{-1}) in standard atmospheric conditions, and C is a dimensionless factor chosen to be 2.0, derived by Buchwitz et al. (*23*), based on the concentration difference of the air parcel before and after entering the source area. The surrounding background is defined as a rectangular box centered at the Permian Basin. We vary the width and length of the surrounding background from 8 to 24 degrees at a 2-degree interval. Wind speed V is taken from the average horizontal boundary layer winds over the source region from ECMWF ERA5 data at 20:00 UTC, which is close to TROPOMI overpass time over Permian basin. Using the mass balance method, we estimate an annual average methane emission rate of 3.2 Tg a^{-1} from the Permian Basin.

The uncertainty of the method (σ_{tot}) is computed as $\sqrt{\sigma^2_{\Delta XCH_4^t} + \sigma^2_{CF}}$ to account for contributions from both ΔXCH_4^t and CF. The uncertainty due to ΔXCH_4^t ($\sigma_{\Delta XCH_4^t}$), dominated by the variations in the background XCH_4^t, is estimated by varying the size of surrounding background region. The uncertainty due to CF (σ_{CF}), primarily contributed by the uncertainty in wind speed, is computed using the empirical equation derived in Buchwitz et al. (*23*) We find σ_{tot} to be 2.0 Tg a^{-1} ($\sigma_{\Delta XCH_4^t}$ = 0.5 Tg a^{-1} and σ_{CF} = 1.9 Tg a^{-1}) in this work.

Text S4 Current status of regulation in the Permian Basin

Oil and gas production on federal lands occur only on the New Mexico portion of the Permian Basin. These lands accounted for 9.6% (398 Bcf) and 8.9% (18 Bcf) of total Permian gas production (https://www.enverus.com/) and gas flaring (https://eogdata.mines.edu/download_global_flare.html), respectively. With the rescinding of the gas capture and fugitive emissions requirements in the BLM's 2016 Methane Waste Prevention Rule, Permian Basin operators with assets on both federal and state lands are now required to meet the state standards only. Both New Mexico and Texas do not have associated gas capture targets and both states permit associated gas flaring in the Permian Basin. Additionally, both states currently do not directly regulate oil and gas methane emissions.

In 2016, the Bureau of Land Management's Methane Waste Prevention Rule (https://www.regulations.gov/document?D=BLM-2016-0001-9126) imposed limits on associated gas venting, flaring and fugitive leaks from new and existing sites operated on federal lands. The BLM's 2018 revision (https://www.govinfo.gov/content/pkg/FR-2018-09-28/pdf/2018-20689.pdf) of the 2016 rule rescinded these requirements, arguing that these rules were unnecessary because the EPA had analogous requirements for fugitive leaks, and venting and flaring are regulated under state requirements. However, the EPA fugitive emissions requirements are less stringent—they focus only on new or modified facilities commissioned in September 2015 and later and do not address gas waste from other existing sites. Furthermore, the EPA recently proposed to revise these requirements (https://www.federalregister.gov/documents/2018/10/15/2018-20961/oil-and-natural-gas-sector-emission-standards-for-new-reconstructed-and-modified-sources), loosening the leak detection and repair frequency and allowing more time to perform repairs of detected leaks. Thus, the vast majority of Permian operations (i.e. existing sites) on both federal and state lands are now required to meet the state standards only.

Both New Mexico and Texas do not have associated gas capture requirements analogous to the requirements in the 2016 BLM rule, and both states currently permit associated gas flaring in the Permian Basin. The Texas Railroad Commission's Statewide Rule 32 (https://texreg.sos.state.tx.us/public/readtac$ext.TacPage?sl=R&app=9&p_dir=&p_rloc=&p_tloc=&p_ploc=&pg=1&p_tac=&ti=16&pt=1&ch=3&rl=32) grants administrative flaring permits that can be renewed for 180 days. Operators can apply for extension to flare beyond the first 180 days and provide additional information on progress made "toward establishing the necessary infrastructure to produce gas rather than flare it." These extensions are routinely granted, primarily because "the operator is waiting for pipeline construction scheduled to be completed by a specified date." Similarly, The New Mexico Administrative Code 19.15.18.12A (http://164.64.110.134/parts/title19/19.015.0018.html) permits venting and flaring of casing-head gas in unlimited quantities within the first 60 days following completion. Exceptions may be granted beyond the first 60 days when venting/flaring appears "reasonably necessary to protect correlative rights, prevent waste or prevent undue hardships on the applicant."

Supplementary figures

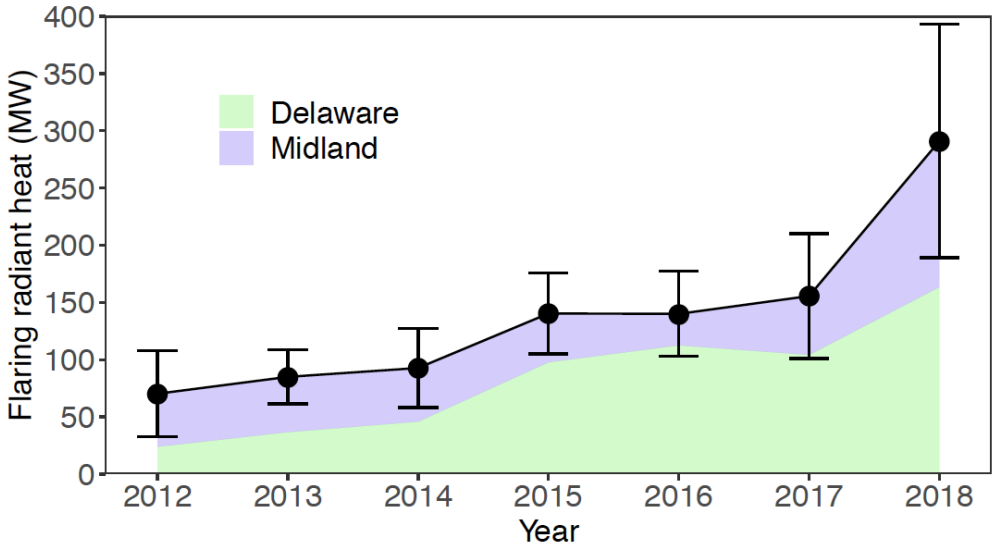

Fig. S1 Annual mean gas flaring radiant heat over the Permian Basin observed by VIIRS from 2012 to 2018. Error bars represent the standard deviation of monthly variations. The blue shading represents the Midland Basin and the green shading the Delaware Basin.

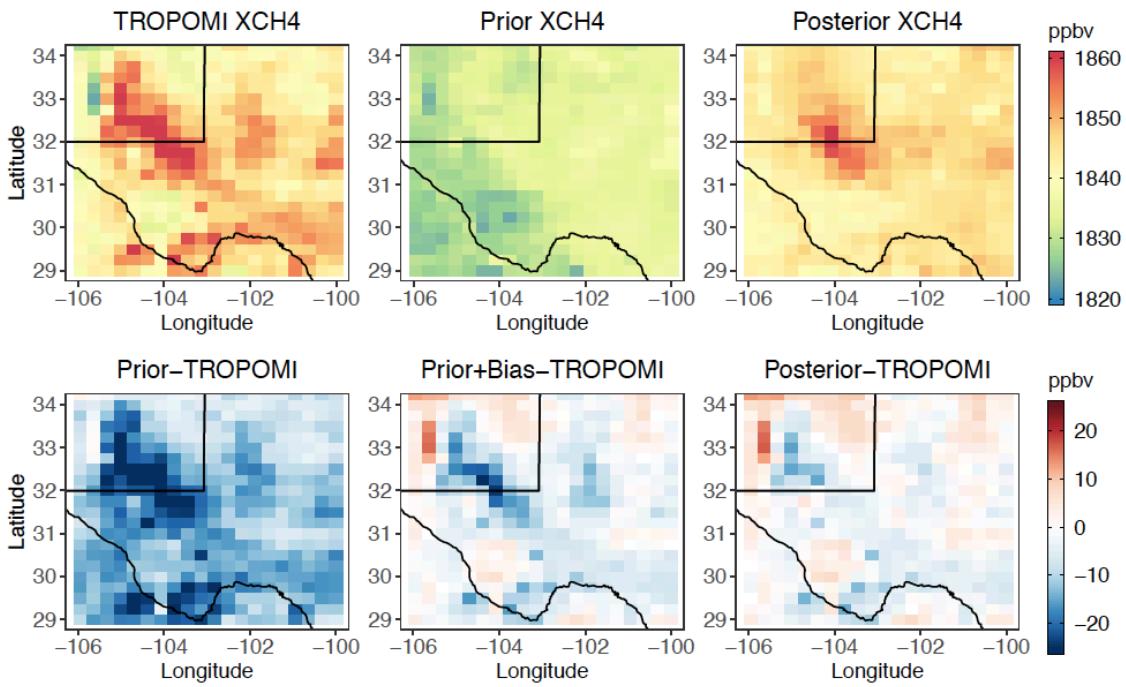

Fig. S2 Observed and simulated XCH_4 over the Permian Basin. The top panels show TROPOMI observations, GEOS-Chem prior simulation, and GEOS-Chem posterior simulation respectively. The bottom panels show the difference between simulations (prior simulation, prior simulation with regional biases corrected, and posterior simulation) and observations. Data are averaged from May 2018 to March 2019.

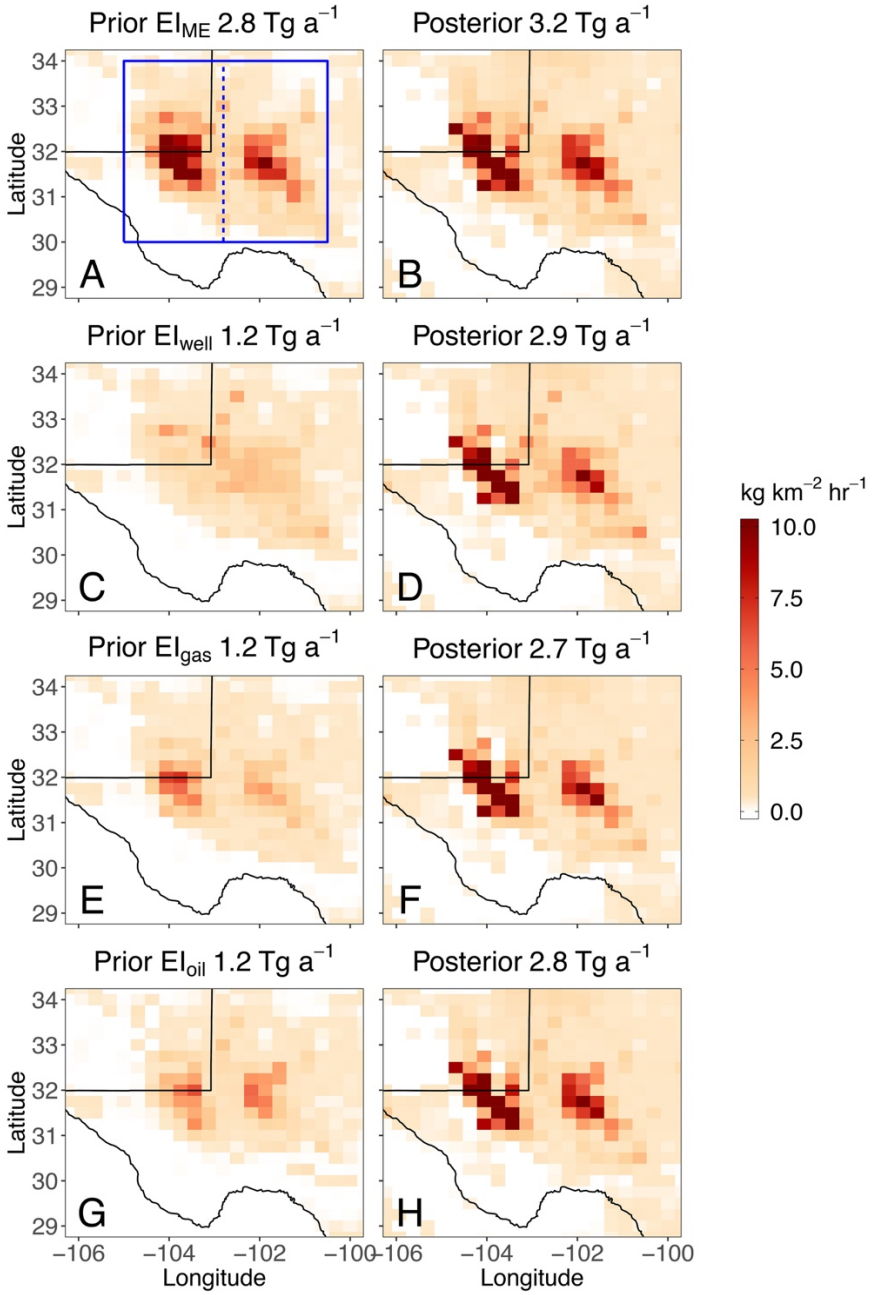

Fig. S3 Spatial distribution of methane emission rates in the Permian Basin in alternative prior emission inventories (A, C, E, G) and the corresponding posterior estimates (B, D, F, H). A, B are for EI_{ME}, C, D for EI_{well}, E, F for EI_{gas}, and G, H for EI_{oil}. The solid blue box encloses the Permian Basin with the two sub-basins to the left (the Delaware) and the right (the Midland) of the dashed line.

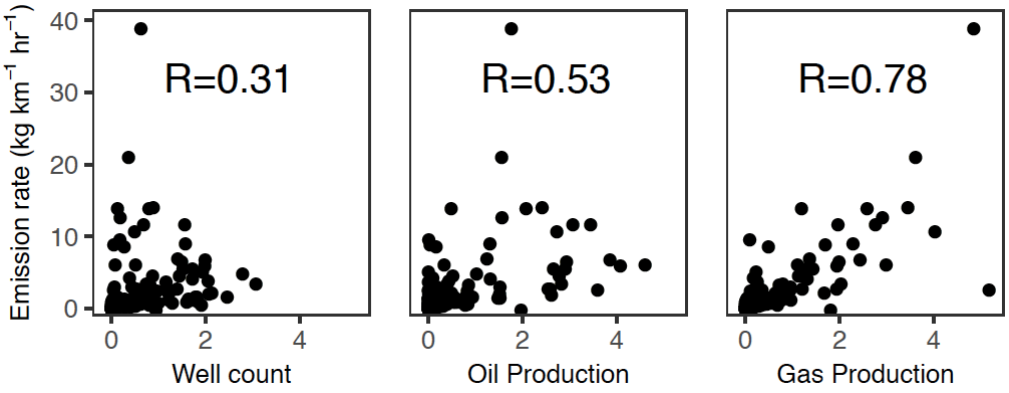

Fig. S4 Spatial correlation between the posterior methane emission rates and O/G production activities for each grid cell. Data for well count, oil production, and gas production are normalized and expressed in %.

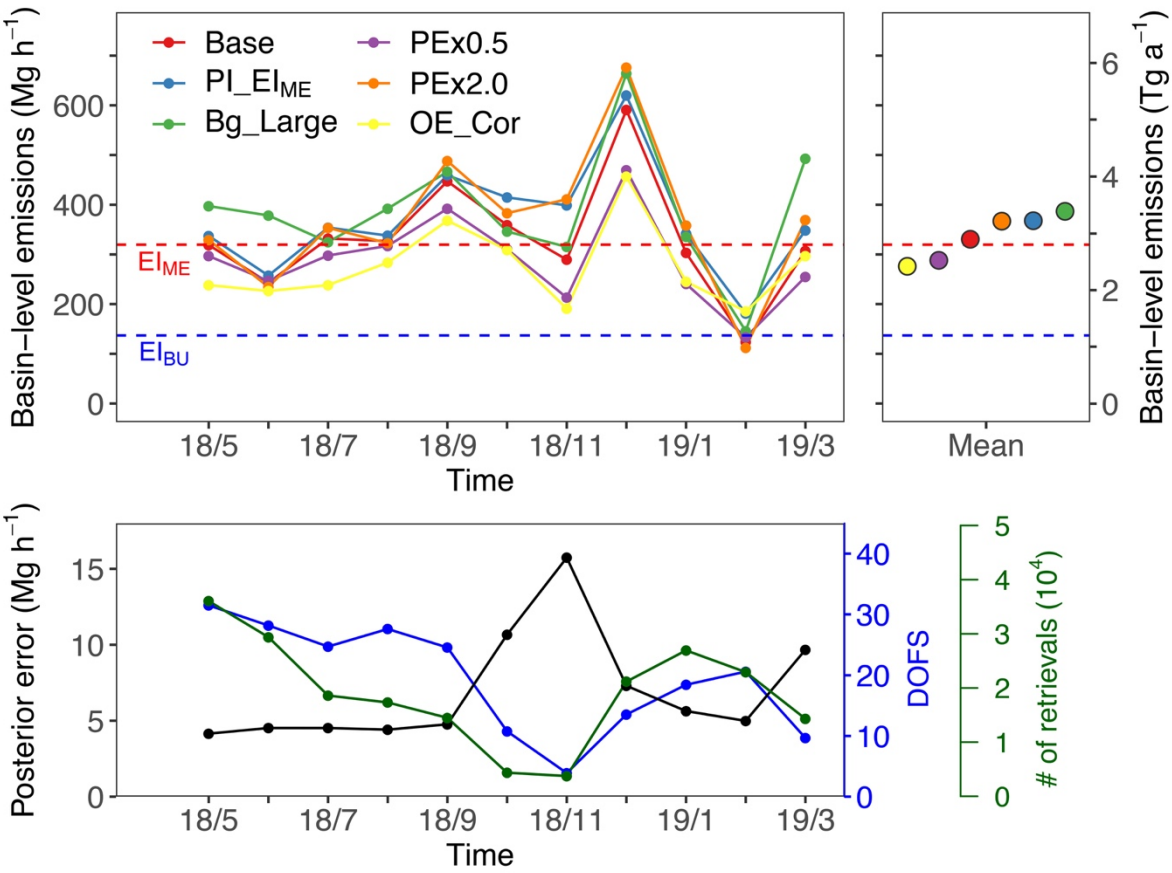

Fig. S5 Monthly methane emission rates estimated by the base and sensitivity inversions (top) and analytical posterior error (bottom). The top panel shows the monthly and mean basin-level methane emission estimates by the base and sensitivity inversions (table S2). Blue and red dashed lines indicate basin-level emissions estimated by EI_{BU} and EI_{ME}, respectively. The bottom panel shows monthly count of successful retrievals used in the base inversion (green), analytical posterior errors for the basin-level methane emissions (black), and corresponding degrees-of-freedom for signals (DOFS) (blue).

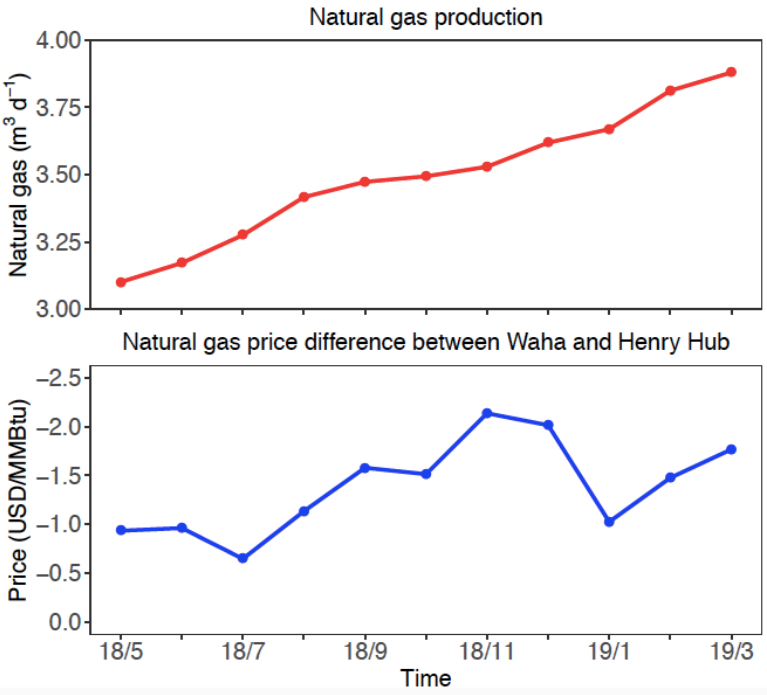

Fig. S6 Monthly natural gas production and price in the Permian Basin. Top: natural gas production in the Permian Basin. Bottom: monthly mean natural gas spot price between Waha (in the Permian Basin) and Henry Hub (benchmark of the North America natural gas market). Note that the price differences (Waha – Henry Hub) are negative, meaning that natural gas is traded below the Henry Hub benchmark within the Permian Basin.

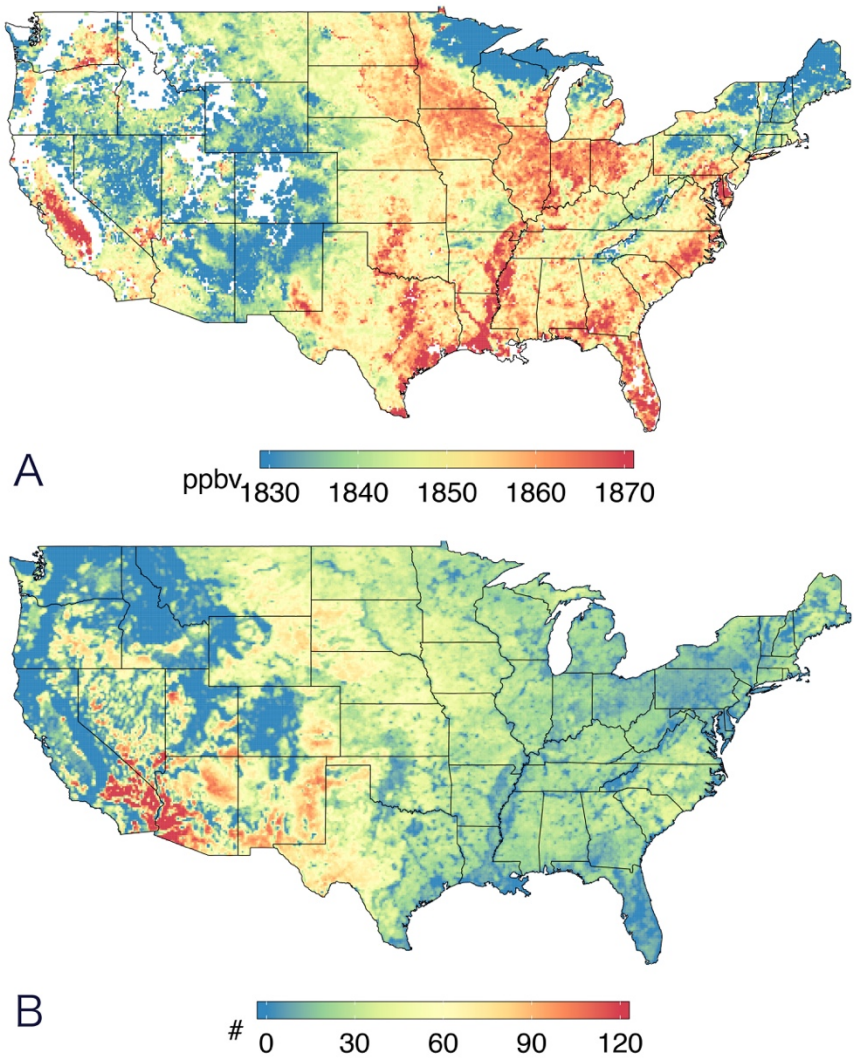

Fig. S7 TROPOMI XCH4 observations over the conterminous U.S. (A) Average column methane mixing ratio (XCH_4) over the conterminous U.S. during the study period. The 11-month average is derived from monthly mean XCH_4 from TROPOMI. (B) Number of days with successful retrievals on the 0.2°×0.2° grid from May 2018 to March 2019.

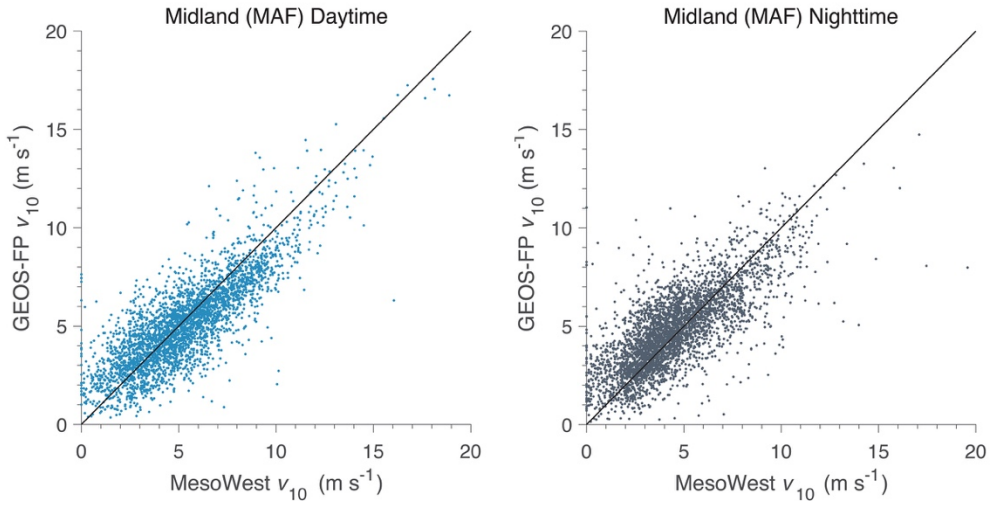

Fig. S8 Evaluation of GEOS-FP wind speed in daytime (left) and nighttime (right). Data are from May 2018 to March 2019. Surface measurements at the Midland Airport (MAF) in the Permian Basin are obtained from MesoWest (mesowest.utah.edu).

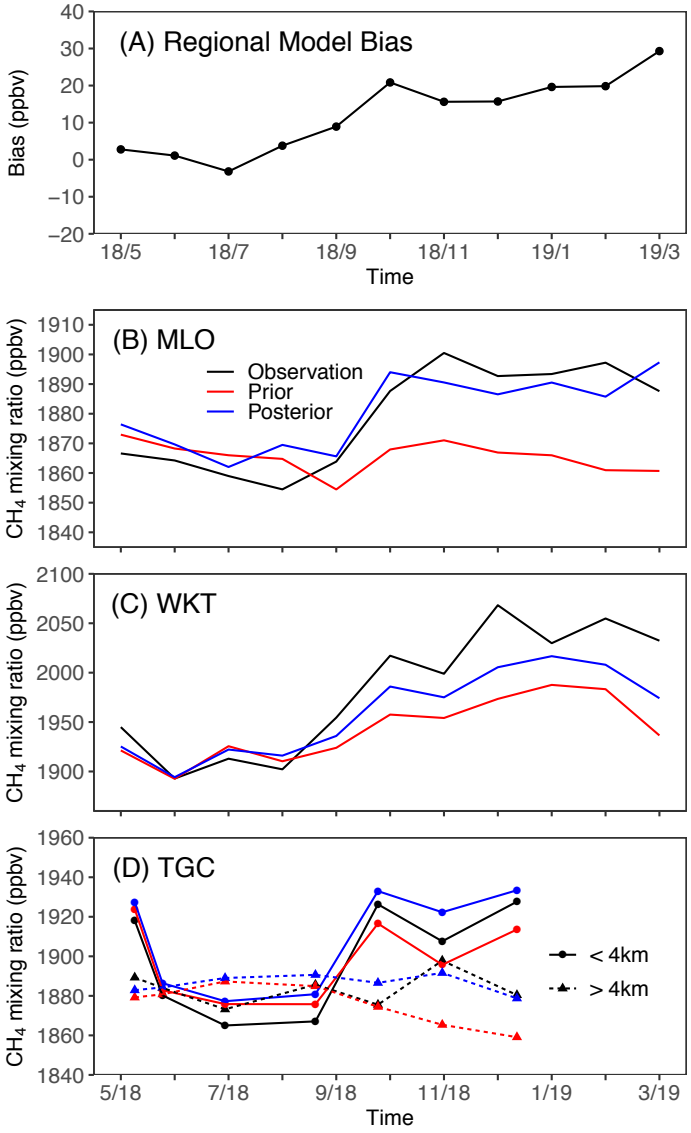

Fig. S9 Regional model biases inferred from the TROPOMI inversion and evaluation with independent observations. (A) monthly regional model biases for the simulated methane column (XCH_4) from the base inversion. (B-D) Evaluation with surface measurements at MLO (B), tower measurements at WKT (C), and aircraft vertical profile measurements ~ 250–8000 m at TGC (D). The bias corrected model results (blue) are computed as the sum of original model results (red) and model biases inferred from the inversion (regional model biases derived from our inversion times a factor of 1.25 to convert the column bias to the free tropospheric bias). We show monthly averages for MLO and WKT, and flight averages above and below 4 km altitude for TGC. This comparison suggests that the regional model bias term introduced in the inversion is effective for correcting background biases resulting mainly from imperfect boundary conditions.

Table S1. Estimates of O/G-related methane emissions reported in previous aircraft-based studies for 11 U.S. O/G producing basins. [a]

	Ref.	Date Sampled (Month/year)	NG production (10^9 m^3 a^{-1})	CH_4 fraction in NG (%)	O/G-related emissions (Tg a^{-1})	Production normalized emission rate (%)
Haynesville	(*26*)	6/2013	80	86	0.63	1.3
Barnett	(*27*)	3 & 10/2013	61	89	0.53	1.4
NE PA	(*28*)	5/2015	60	95	0.16	0.4
NE PA	(*26*)	7/2013	N/A	95	0.11	0.3
San Juan	(*12*)	4/2015	29	83	0.50	3.0
Fayetteville	(*29*)	10/2015	26	97	0.24	1.4
Fayetteville	(*26*)	7/2013	N/A	97	0.31	1.9
Bakken	(*30*)	5/2014	20	47	0.24	3.7
Uinta	(*31*)	2/2012	12	89	0.48	6.6
Denver Basin	(*32*)	5/2012	10	79	0.17	3.1
West Arkoma	(*26*)	7/2013	4	96	0.23	9.1
Bakken	(*24*)	4/2015	13	47	0.25	5.4
Barnett	(*24*)	4/2015	44	87	0.40	1.5
Denver Basin	(*24*)	3/2015	14	77	0.16	2.1
Eagle Ford [b]	(*24*)	4/2015	56	N/A	0.73	2.5
west			32	77	0.36	2.0
east			24	68	0.37	3.2
Haynesville	(*24*)	4/2015	54	90	0.37	1.0
SW PA	(*25*)	8 & 9/2015	29	88	0.19	1.1
11-basin sum [c]			322	N/A	3.71	1.9
Permian	This study	5/2018-3/2019	128	80	2.7	3.7

[a] Data are taken from a summary by Alvarez et al. (*7*) except for those from Peischl et al. (*24*) and Ren et al. (*25*).

[b] Emissions from Eagle Ford are reported separately as west and east sub-basins (*24*), based on which we compute the data for the entire basin.

[c] 11-basin sum is computed with latest measurements if multiple studies exist for a specific basin. Therefore, shaded rows are excluded in calculating the 11-basin sum.

Table S2. Total basin-level methane emission estimates from an ensemble of sensitivity inversions perturbing a variety of inversion parameters.

	Inversion	Basin methane emissions ($Tg\ a^{-1}$)
	Base inversion [a]	2.9
	Sensitivity inversions perturbing prior emissions [b]	
PI_EI_{ME}	EI_{ME} as prior emissions	3.2
PI_EI_{oil}	EI_{oil} as prior emissions	2.7
PI_EI_{gas}	EI_{gas} as prior emissions	2.7
PI_EI_{well}	EI_{well} as prior emissions	2.9
	Sensitivity inversions perturbing the size of spatial domain	
Bg_Large	27°–36°N, 98°–108° W	3.4
	Sensitivity inversions perturbing error covariance specifications	
PE×2	Double prior error	3.2
PE×0.5	Halve prior error	2.5
OE_Cor	Specify observational error correlations [c]	2.4

[a] Base inversion is performed over a domain in 29°–34°N, 100°–106° W and uses EI_{BU} as prior information. Both $\mathbf{S}_O$ and $\mathbf{S}_A$ are taken to be diagonal. Prior errors are specified as the absolute difference between EI_{BU} and EI_{ME}. Observational errors are specified following the residual error method (*43*).

[b] Spatial distributions of these prior emission inventories and corresponding posterior estimates are shown in fig. S3.

[c] $\mathbf{S}_O$ is specified following Cusworth et al. (*44*) by assuming 4 ppbv model errors with a spatial correlation length of 40 km and independent instrument errors.